Application of Low-Fidelity Methods to eVTOL Propeller Icing and Performance Degradation

Aishwerya Gahlot[1]
aishwerya@gatech.edu
Graduate Researcher
Georgia Institute of Technology
Atlanta, GA, USA

Paul H. von Hardenberg[2]
paul.h.vonhardenberg@nasa.gov
Aerospace Research Engineer
NASA Glenn Research Center
Cleveland, OH, 44135, USA

Lakshmi Sankar[3]
lsankar@ae.gatech.edu
Regents Professor
Georgia Institute of Technology
Atlanta, GA, USA

ABSTRACT

The performance of electric vertical takeoff and landing (eVTOL) vehicles can be significantly degraded by ice accretion on propeller blades during flight through supercooled clouds. While high-fidelity icing tools are available, their computational cost limits rapid design-space exploration. This study presents a low-fidelity, modular framework that couples blade element momentum theory (BEMT) with two-dimensional icing models to predict both ice accretion and performance degradation. Experimental data from NASA Glenn's Icing Research Tunnel for 28-inch and 36-inch diameter carbon fiber propellers serve as validation for the methodology. Ice shapes for both rime and glaze conditions are simulated using single- and multi-step approaches with LEWICE and GTICE2D. Comparisons with tunnel data demonstrate that the approach captures reasonably well the trends in impingement limits, ice thickness, and collection efficiency, while preserving computational efficiency. The results highlight the utility of low-fidelity tools for assessing the effects of icing in early-stage design and operational analysis of eVTOL propulsion systems.

Keywords: propeller icing, eVTOL, low-fidelity methods, blade element momentum theory, ice accretion, LEWICE, GTICE2D, performance degradation.

INTRODUCTION

Over the past several decades, significant progress has been made in the physics-based modeling of rotor blades for helicopter, eVTOL, and UAS applications. A variety of low-, mid-, and high-fidelity tools are now available for predicting rotor performance in hover, forward flight, and various maneuvers. These advancements have been greatly supported by high-quality wind tunnel and flight test data [Ref. 1-5]. These tools are reaching a level of maturity that allows them to be used in the design and certification of new rotorcraft and UAS systems, as well as in improving legacy systems.

Mission critical operations of next generation eVTOL and UAS systems would require these vehicles to operate in adverse weather conditions including light rain, fog, and/or icing. These conditions significantly impact vehicle availability, reliability, and affordability. Consequently, there is a growing need to extend classical blade element theory-based tools and advanced CFD analyses to assess the effects of rain and icing on system performance. A need also exists for high quality experimental data for representative rotor configurations under dry and icing conditions for the validation of these tools.

The Icing Research Tunnel (IRT) at NASA Glenn Research Center has a long-standing and highly regarded history in both fundamental and applied research on ice accretion and its impact on performance. The center has developed extensive test data for fixed and rotary-wing icing phenomena, as well as analytical and computational tools such as LEWICE [6], which are widely used by researchers globally to validate their models [Ref. 7-9].

Over the past two years, a general-purpose propeller test stand has been developed at the IRT to conduct fundamental icing research on electrically driven propellers. Three carbon fiber propellers, with diameters of 0.610 m, 0.711 m, and 0.914 m (24, 28, and 36 inches), have been systematically studied under various operating and cloud conditions. These propellers utilize NACA 0012 airfoil sections, with available chord and twist angle distributions provided in Reference 10. The propeller test stand, equipped with the 36" diameter propeller and installed in the IRT test section, is shown in Figure 1. The test campaign involved parametric sweeps of droplet characteristics and rotor operating conditions to assess their effects on ice accretion, including ice thickness, mass, impingement limits, and ice type (glaze vs. rime). Additionally, propeller performance degradation, measured through changes in torque over time, and ice shedding events, were captured and recorded. Ice shapes from the test were reviewed for their repeatability, correctness of trends, and sensitivity to parameter variations and are currently being used to support the development of icing computational tools. [Ref. 10-11]

Figure 1. NASA's eVTOL Propeller Icing Test Stand Installed in the Icing Research Tunnel

RESEARCH OBJECTIVES

As eVTOL propellers are designed to operate across a broad spectrum of conditions, there is an increasing need for tools that can rapidly explore the design and operating space and assess performance impacts. Therefore, the objective of the present study is to develop rapid, low-fidelity computational models for ice accretion on propellers in climb and/or forward flight, as well as the resulting performance degradation. A modular approach has been adopted, allowing for the independent use and testing of complementary propeller modeling and ice accretion prediction tools.

OVERVIEW OF THE METHODOLOGY

The major steps of the present methodology, represented in the flow chart in figure 2, are as follows.

1. The clean/dry propeller is analyzed first. A combined blade element-momentum theory (BEMT) is used to estimate the induced inflow and swirl while accounting for tip loss. Validation of the analysis for dry rotors is done through comparisons with test data. The propeller performance based on BEMT methodology is briefly described in Appendix A.

2. This approach yields effective angles of attack and velocity at any radial location on the rotor blade for a particular operating condition. A table look-up of lift and drag coefficients as a function of angle of attack is used. The table look-up data may come from experimental measurements or computational tools such as XFOIL or CFD. XFOIL was used to generate the loads table in this analysis.

3. At seven selected locations on the rotor, for which experimental measurements of ice shapes are available, ice accretion is predicted for a user-specified time duration based on the experimental operating conditions. The ice accretion modeling requires the prediction of water droplet collection efficiency, surface skin friction distribution, transition location, and ice growth. Lagrangian tools, such as LEWICE, as well as Eulerian approaches (found in tools like FENSAP and GTICE2D [12-13]),

may be used to predict collection efficiency. Classical or extended Messinger ice growth models may be applied. The ice accretion model called GTICE based on extended messenger model was implemented by Kim [13]. A modified version, described in Appendix B, has been used in the present study. LEWICE based ice accretion was also performed for comparison purposes.

4. The performance impact is estimated by repeating the propeller analysis with new 2-D airfoil tables for the iced airfoil shapes.

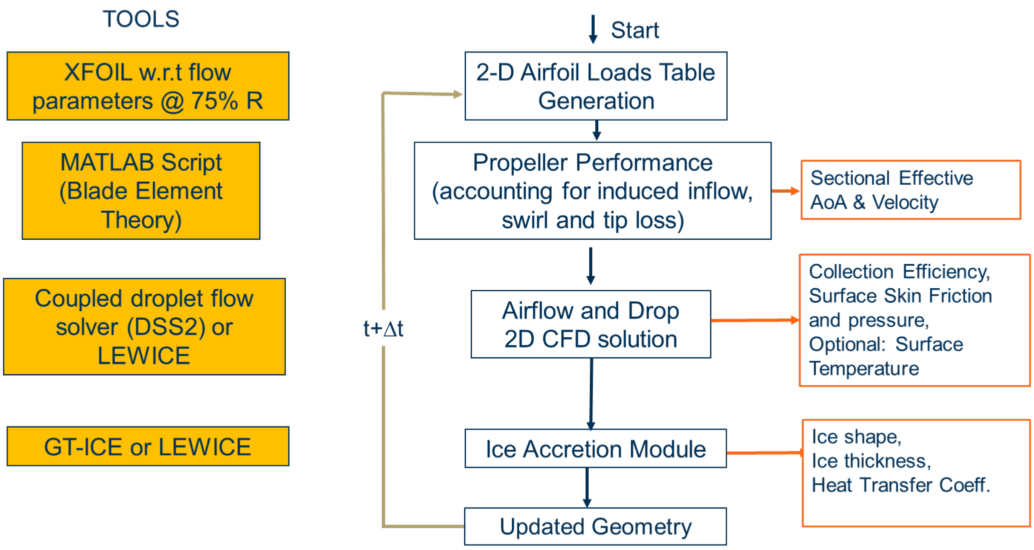

Figure 2. Methodology of the Low-Fidelity Approach

Automated MATLAB scripts have been developed that call the underlying tools in sequence and prepare the necessary input data (in human readable text format) for the individual modules. At the time of writing, LEWICE or GT-ICE (2D) may be used with customized versions of the MATLAB script. Steps 1 through 3 may be repeated for additional ice accretion time intervals in a multi-step icing approach.

RESULTS AND DISCUSSION

The first step in this approach is validating the performance of the 4-bladed clean propellers (28” and 36” diameter propellers) from BEMT methodology. Figures 3 and 4 show the predictions from the present methodology (Appendix A) for the 36” and 28” diameter rotors. NACA 0012 airfoil load characteristics were estimated using XFOIL, and the lift coefficients were corrected for compressibility effects at each radial location using the Prandtl-Glauert method. The BEMT analysis gives acceptable results over the advance ratio J range between 1.5 and 2.4, where J is defined in propeller notation in terms of the forward velocity (or climb velocity) V, rotor revolutions per second n, and the rotor diameter D as J = V/nD. Several factors contribute to the observed deviations from test data. A possible source of discrepancy is the limited range of Reynolds numbers represented in the loads table, which does not fully encompass the range of advance ratios considered in the analysis. Despite this limitation, the cases of primary interest for the 28in propeller (runs RA3683 and RA3701, which differ only in temperature) correspond to regions where good agreement between measurements and predictions was achieved.

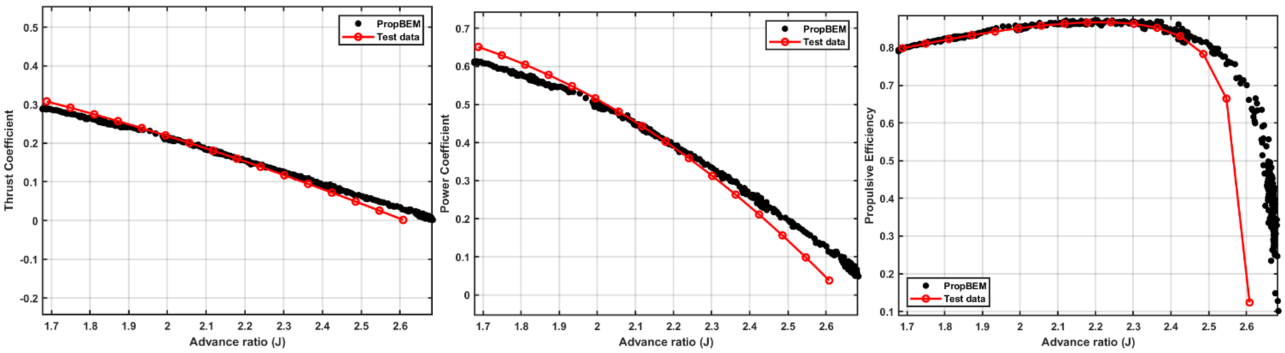

Figure 3. Comparison of the Blade Element-Momentum Theory predictions with NASA Test data for the 36" Diameter Propeller.

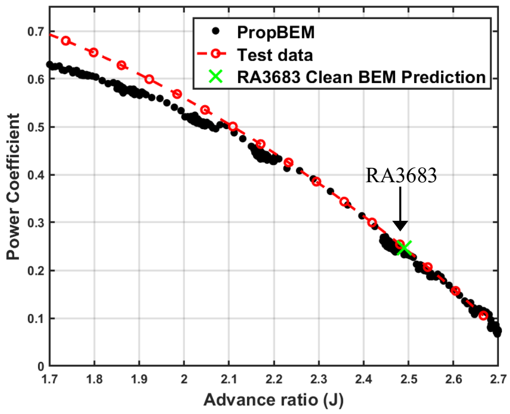

Figure 4. Comparison of the Blade Element-Momentum Theory predictions with NASA Test data for the 28" Diameter Propeller.

Rime Ice Shape Comparisons

Repeatable, high-quality ice shapes are available for the 28-inch propeller at a specified operating condition, referred to as RA3683 [Ref. 10]. Run RA3683 corresponds to a rime ice condition where the impinging droplets freeze upon impact resulting in an ice shape that more closely follows the contour of the airfoil. Images of the ice accretion from run RA3683 are provided in Figure 27 in Appendix C. The parameters for Run RA3683 are described in Table 1.

Table 1. Flow parameters for Run RA3683.

Forward Speed, V_∞ (knots)	Forward Speed, V_∞ (m/s)	Total Temperature, $t_{\infty,0}$ (°C)	Drop Diameter, δ (μm)	LWC, (g/m^3)	Icing time, τ (sec)	RPM (rev/min)	Propeller Diameter (in)	Advance Ratio, J
87	44.8	-15	15	0.55	180	1516	28	2.49

At this condition, corresponding to an advance ratio of approximately 2.5, the data presented in Table 2 is extracted from the BEMT propeller analysis for later use in the icing analysis. In this table, the effective velocity is the magnitude of the vector sum of in-plane components (section velocity and swirl), and the component normal to the rotor disk (forward velocity and axial induced velocity).

Table 2. Sectional Effective Velocities and Angles of Attack at selected sections for the 28” propeller for Run RA3683.

r/R	c/R	Effective Velocity (m/s)	Effective Angle of Attack (deg)
0.40	0.248	50.33	0.44
0.50	0.267	53.30	1.14
0.60	0.271	56.63	1.58
0.70	0.254	60.65	2.00
0.75	0.238	62.36	2.06
0.80	0.217	64.53	2.18
0.90	0.164	68.58	2.15

Ice accretion simulations were conducted for various time steps to assess the variability in ice shapes. Both single-shot and multi-shot approaches were applied to run RA3683, utilizing both GTICE2D and LEWICE. In the multi-shot approach, the flow solution is updated after each step. For example, in a 4-step simulation, the total icing time of 180 seconds is divided into four equal intervals of 45 seconds, with the flow solution updated every 45 seconds. Similarly, in an 8-step simulation, the flow solution is updated every 22.5 seconds.

For both GTICE2D and LEWICE simulations, the effective velocity and effective angle of attack, as outlined in Table 2, were applied. In GTICE2D, collection efficiency, surface pressure, and skin pressure data are computed from a two-way coupled 2D CFD flow solver tightly coupled with an Eulerian droplet transport model. LEWICE employs a potential flow solver for surface pressure calculations and Lagrangian droplet transport to compute collection efficiency.

The resulting ice shapes from the single-shot and multi-shot (4-step) simulations using the GTICE2D solver are presented in Figures 5 and 6. Figures 7 and 8 compare the ice shapes generated by GTICE2D with those produced by LEWICE for the single-shot and multi-shot (8-step) approaches. While both tools capture the impingement limits well, GTICE performs somewhat better in predicting the maximum ice thickness at each radial section for single step simulations. More detailed features emerge when the simulation is repeated with flow updates in the 8-step approach.

One contributing factor to the mass discrepancy in Figure 7 may be the assumed ice density. GTICE uses 880 kg/m³ for rime ice and 917 kg/m³ for glaze ice (Appendix B), whereas LEWICE applies a fixed value of 917 kg/m³ for all cases. This could partly explain the lower total mass in the LEWICE results. Additionally, GTICE employs the Extended Messinger model, which solves coupled PDEs for energy and mass with temperature variation through the ice and water layers (Eqs. 12-13) and uses Stefan’s equation for ice growth (Eq. 15). LEWICE, by contrast, uses the Classical Messinger model with simplified energy balance and prescribed freezing based on impingement. These modeling differences likely contribute to the discrepancies in ice thickness and mass.

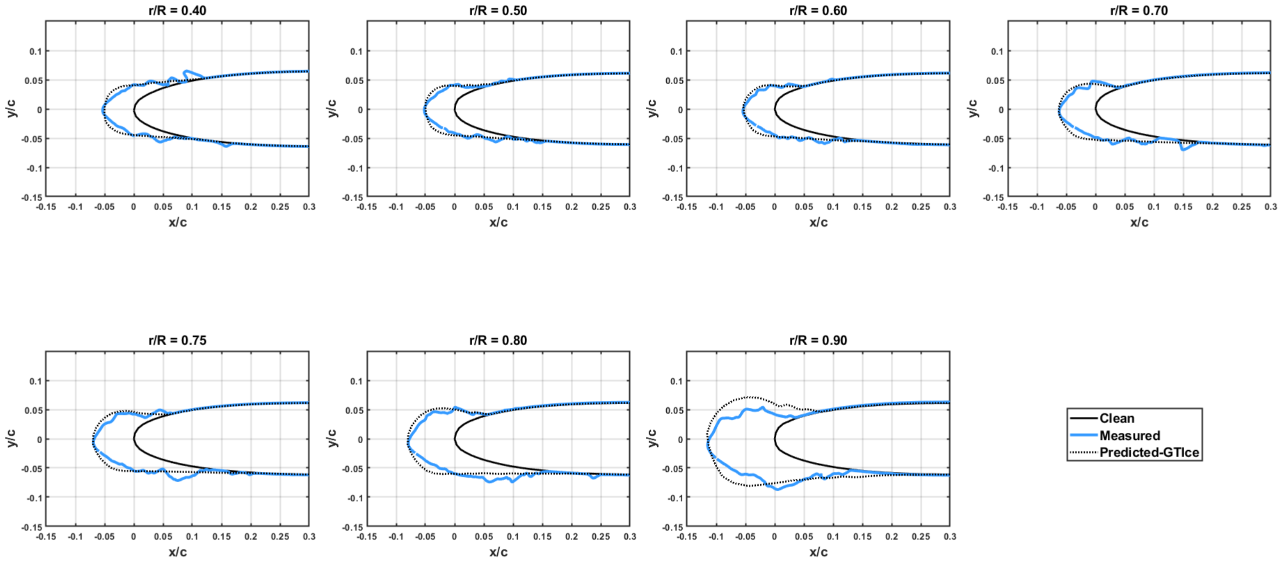

Figure 5. GTICE Predicted Ice shapes for RA3683 (single step).

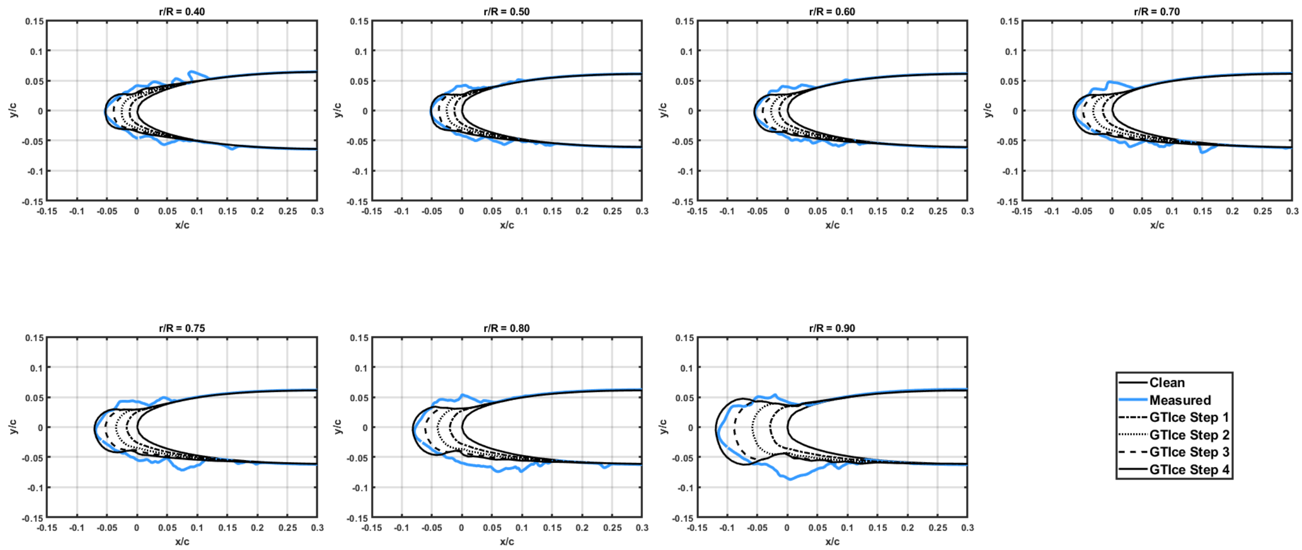

Figure 6. GTICE Predicted Ice shapes for RA3683 (4-steps).

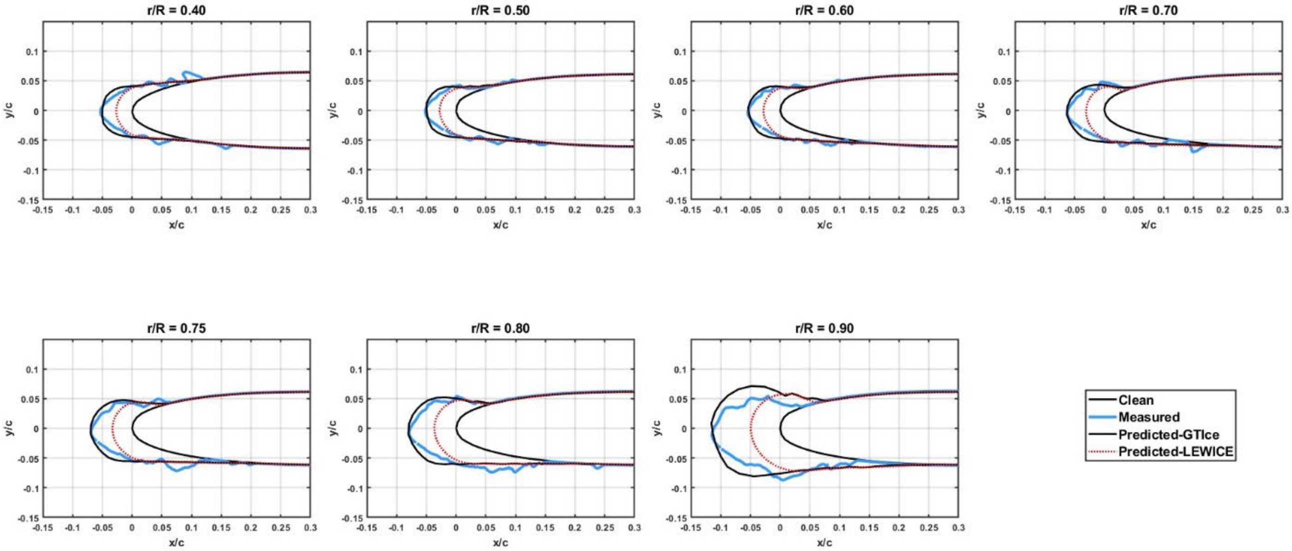

Figure 7. GTICE-predicted ice shapes compared with LEWICE-predicted ice shapes for RA3683 (single-step).

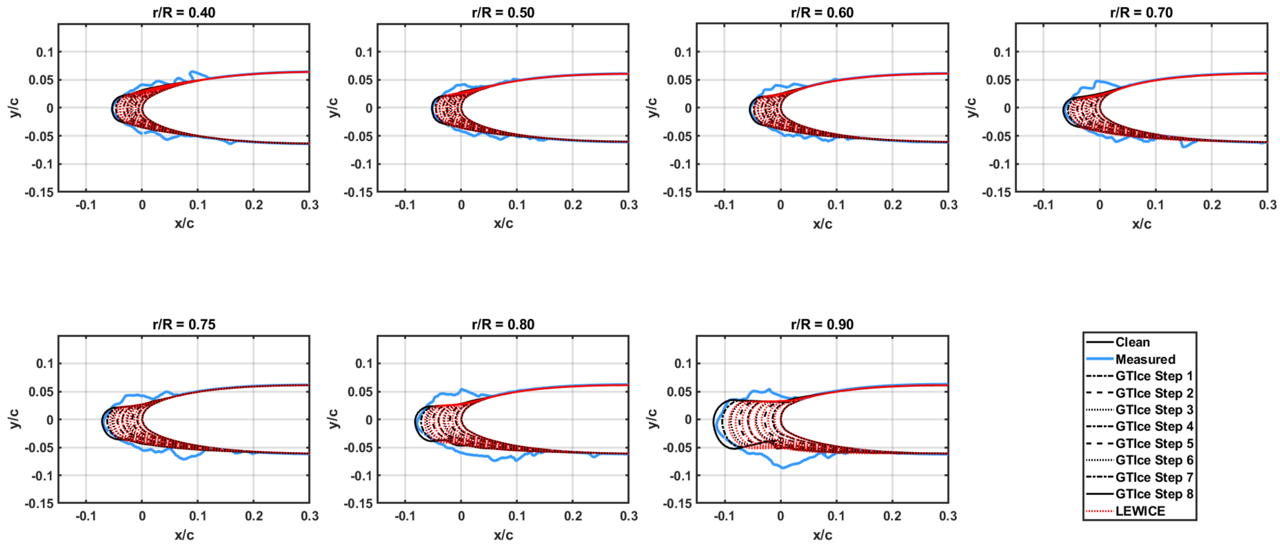

Figure 8. GTICE-predicted ice shapes compared with LEWICE-predicted ice shapes for RA3683 (8-step).

Figure 9 compares the collection efficiency computed by both tools. The maximum collection efficiency at the stagnation point is well captured by both GTICE and LEWICE. The estimated collection efficiency at the stagnation point for the 75% radial location, as reported in Reference 10, is 0.88, while both tools predict it to be approximately 0.85 using the single-step approach and 0.86 using the multi-step approach.

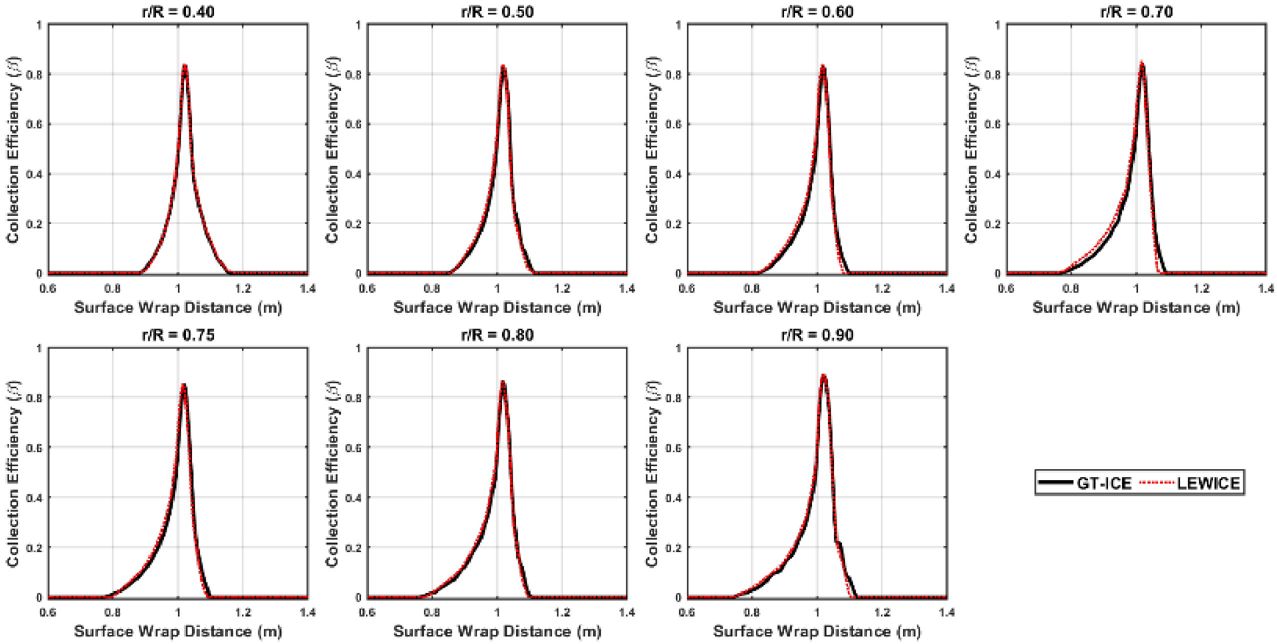

Figure 9. Comparison of collection efficiency (single step) computed by GTICE and LEWICE for Run RA3683.

Glaze Ice Shape Comparisons

A similar analysis was performed for run RA3701 to evaluate the method at glaze ice conditions. The only difference between the two runs (RA3683 and RA3701) is the operating temperature, which is a crucial parameter in determining whether the ice formation will be rime or glaze, as well as the ice thickness. RA3701 represents a glaze ice case with an operating temperature of -3°C, keeping other flow parameters the same as RA3683 as shown in Table 2 below. Images of the ice accretion from run RA3701 are provided in Figure 28 in Appendix C.

Table 3. Flow parameters for Run RA3701

Forward Speed, V_∞ (knots)	Forward Speed, V_∞ (m/s)	Total Temperature, $t_{\infty,0}$ (°C)	Drop Diameter, δ (μm)	LWC, (g/m^3)	Icing time, τ (sec)	RPM (rev/min)	Propeller Diameter (in)	Advance Ratio, J
87	44.8	-3	15	0.55	180	1516	28	2.49

The figures 10 and 11 are the ice shape comparisons corresponding to the RA3701 glaze ice case with the measured data. The overall thickness and the impingement limits are well captured by the single shot approach, however the shapes have a smoother surface. Some of the rough surface features emerge in the multi-shot approach, which are more representative of the roughness caused by ice accretion. Figure 12 compares the multi-step LEWICE simulations with the 4-step GT-ICE predicted ice shapes. While the LEWICE-predicted ice shapes underestimate overall ice thickness, they are comparatively more representative of ice-based surface roughness.

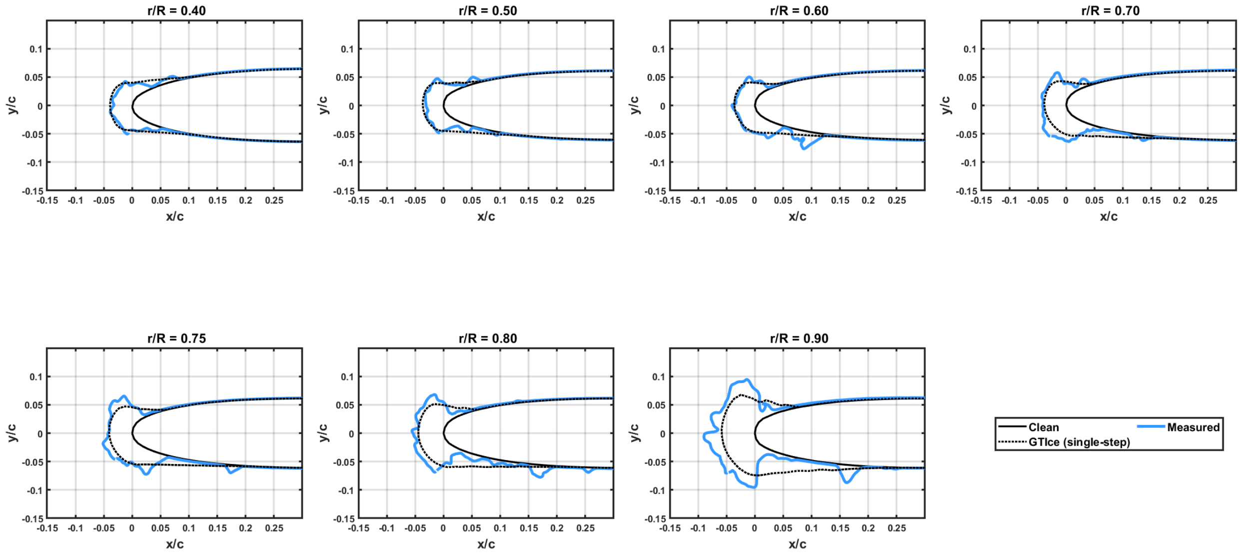

Figure 10. GTICE Predicted Ice shapes for RA3701 (single step).

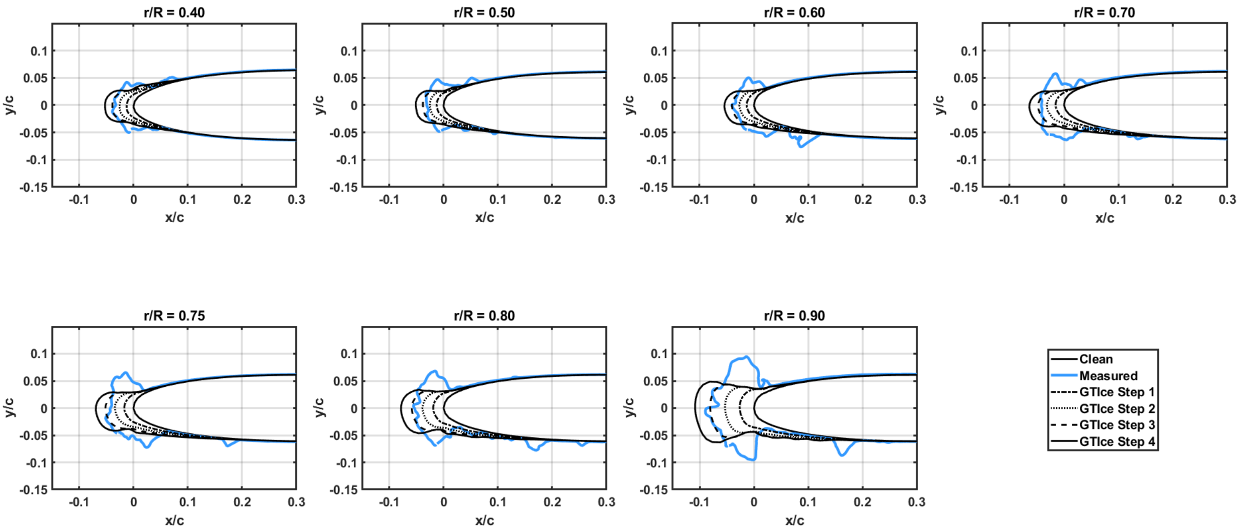

Figure 11. GTICE Predicted Ice shapes for RA3701 (multi-step).

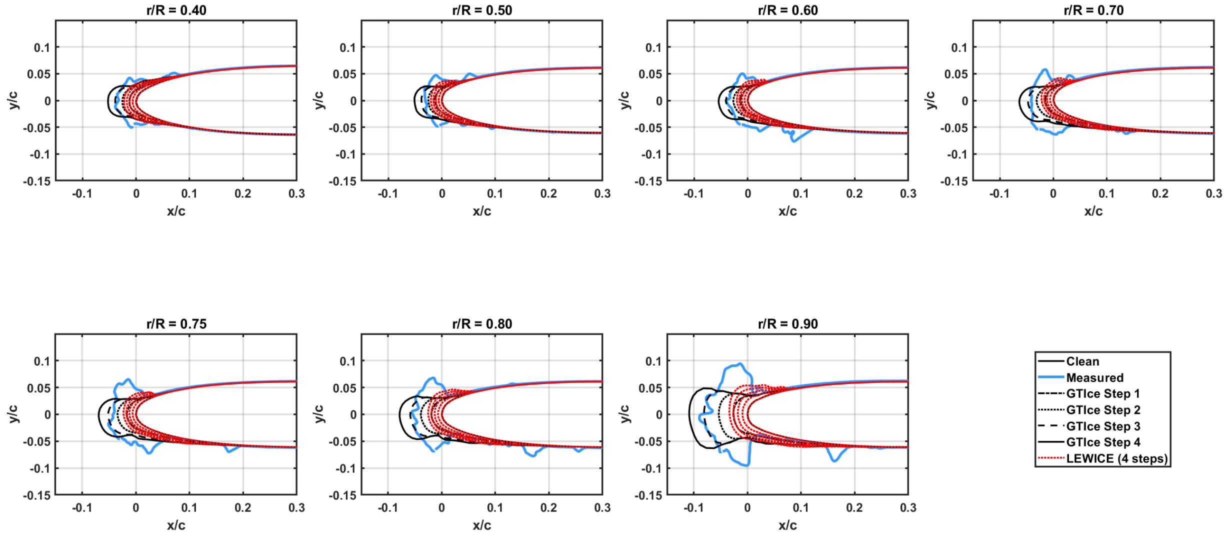

Figure 12. GTICE-predicted ice shapes compared with LEWICE-predicted ice shapes for RA3701 (4-step).

Measured and Predicted Performance of the Iced Propeller

The experimental torque measurements for the rime and glaze ice cases are presented in Figures 13 and 14, respectively. Measurements recorded between -1 and 0 minutes represent the "clean" propeller performance prior to the activation of the spray. These clean measurements were averaged and used to calibrate the propeller's performance predictions by adjusting the collective pitch.

For the rime ice case (RA3683), the clean propeller shows an average torque of 5.614 N-m, corresponding to a torque coefficient CQ of 0.035 and a power coefficient CP of 0.222 at an RPM of 1516. To match this averaged torque in the clean and iced propeller analysis predictions, a collective pitch of 16.7° was employed.

The Blade Element Momentum Theory (BEMT) prediction for the clean propeller showed excellent agreement with the experimental data, matching the measured torque within 0.1%, at a collective pitch of 16.7 degrees. It should be noted that only torque measurements were available from the experiment; therefore, the computational analysis was trimmed to match torque rather than thrust. Following this calibration, the BEMT-based clean rotor performance is considered a validated baseline for comparing the icing effects in the next section.

Similarly, for the glaze ice case (RA3701), the clean propeller exhibited an average torque of 5.422 N-m between −1 and 0 minutes, corresponding to a CQ of 0.0357 and a CP of 0.2245 at the same RPM. A collective pitch of 16.65° was used to match the experimental torque value. The slight difference in clean performance between the two cases is attributed to the change in temperature and likely minor deviations in tunnel speed, typically within ±0.25 knots, and is considered negligible, falling well within the bounds of measurement uncertainty. However, significant differences were observed during icing. As can be seen from the figures 15 and 16 below, as ice accretion progresses, an increasing amount of torque/power is required to maintain the rotor at a constant RPM.

For the rime ice case, after three minutes of ice accretion, the experimental torque increased to 6.47 N-m, representing a 15.28% rise relative to the clean propeller. Whereas after three minutes of glaze ice accretion, the torque increased to 7.13 N-m, corresponding to a 31.43% increase relative to the clean propeller, which is more than double the rise observed in the rime ice case.

It is also worth noting that although the collective pitch and RPM were held nearly constant during the experiment, in practical operations, collective would typically be increased to maintain thrust under icing conditions. Consequently, the true performance loss or power penalty in flight may be greater than indicated by the experimental data, emphasizing the need for further investigations to study the impact of ice accretion on eVTOL performance.

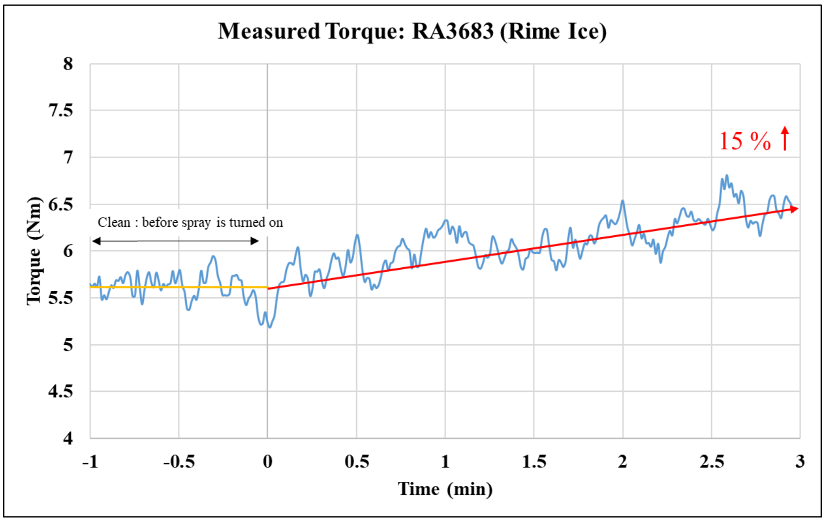

Figure 13. Torque Measurements for RA3683 Rime Ice Case

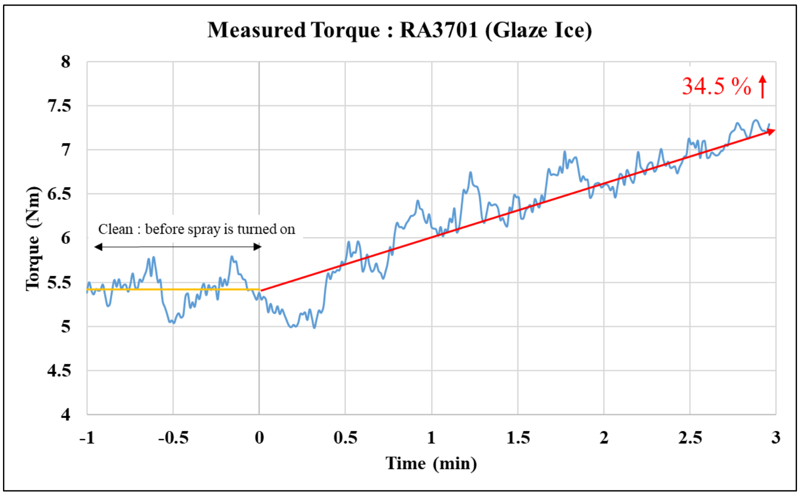

Figure 14. Torque Measurements for RA3701 Glaze Ice Case

To evaluate the degradation in aerodynamic performance resulting from ice accretion, ice shapes generated from both single-step and four-step GT-ICE simulations at the 75% span location were utilized. It is a standard practice within the rotorcraft community to approximate the aerodynamic behavior of the entire blade using the characteristics of the 75% span section. The predicted ice shapes were subsequently analyzed using XFOIL to develop updated aerodynamic load tables: a single load table for the final ice shape in the single-step case, and separate load tables for each intermediate ice accretion stage in the four-step analysis.

A progressive increase in drag and a corresponding loss of lift were observed in the drag polar comparison between the clean airfoil and the iced airfoils, with the degradation becoming more pronounced as ice accretion advanced, as illustrated in figure 15 below representative of performance degradation for the rime ice case.

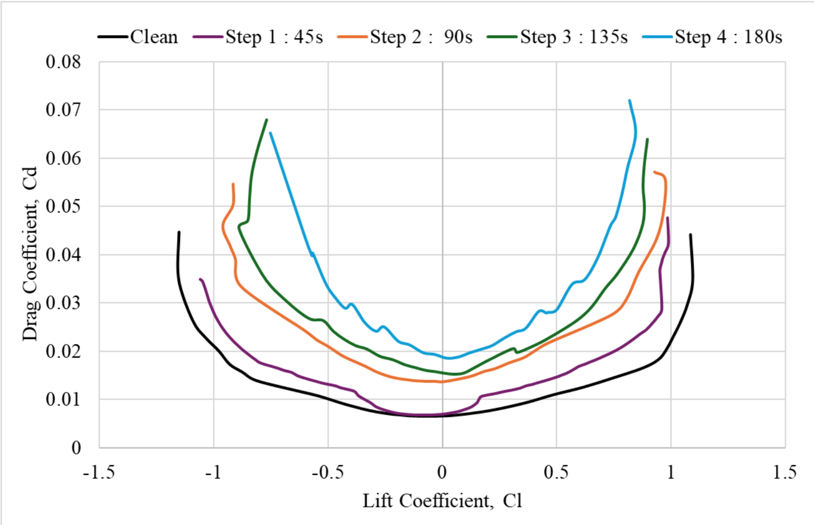

Figure 15. Drag polar at the 75% span location, showing the progression from clean to 3 minutes of ice accretion for the simulated RA3683 case.

Figure 16 shows the performance degradation prediction from the simulated ice shapes and performance analysis performed using BEMT with the updated drag polars. At the end of 3 minutes of icing, the predicted rise in torque was found to be 14.07% , the incremental values are also shown in the orange triangular markers, whereas the experiment observed a 15% rise. Additionally, the efficiency dropped by 16% and a thrust loss of 5% was also predicted, however thrust measurements are not available to make a comparison with experiment. Similar trends were seen with the single shot approach, shown with the green square marker, predicting a 13.97% rise.

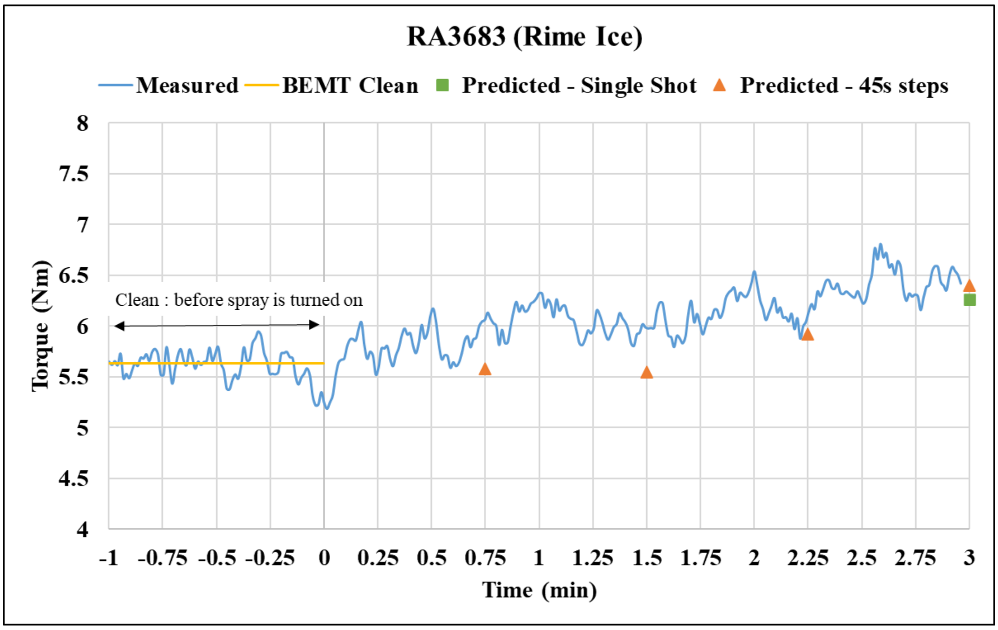

Figure 16. Comparison of measured torque with the predicted increase in torque for icing case RA3683.

Although the predicted torque appears unchanged during the initial accretion steps at 45 and 90 seconds, this does not accurately reflect the underlying performance degradation. In these cases, the rise in profile power is relatively small compared to other power components. Additionally, because thrust is not held constant, the associated thrust loss leads to a decrease in induced power, effectively masking the increased power demand due to icing. However, when the profile power component is isolated, a gradual increase is observed as ice accretion progresses, driven by the rise in drag, as shown in Figure 17. As noted earlier, under in-flight conditions where thrust must be maintained, both parasite and induced power components would also increase.

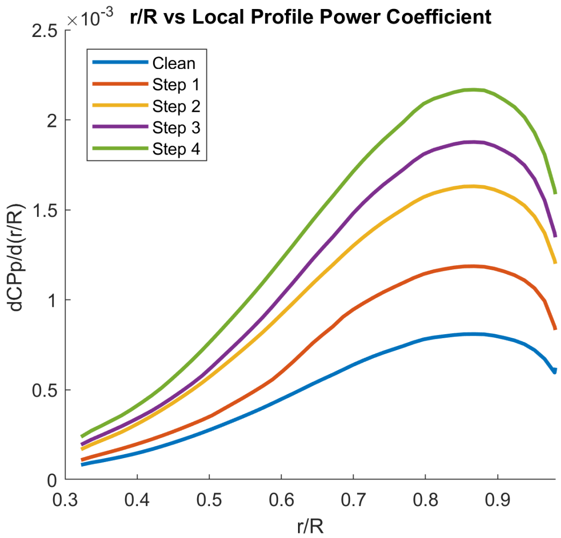

Figure 17. Spanwise distribution of the local profile power coefficient as ice accretion occurs in 45-second intervals.

The performance degradation associated with glaze ice accretion was also evaluated against experimental data, as illustrated in Figure 18. The simulation predicted a 19% increase in torque after 3 minutes of ice accumulation, which is significantly lower than the experimentally observed increase of 34.5%. This significant discrepancy may be attributed to the predicted glaze ice shapes being considerably smoother than the experimental ice shapes, and to the simulated glaze ice shapes failing to capture the abrupt, horn-like features evident in the experimental results. Such surface roughness and flow -separating features of the glaze ice shape in the experimental case would be expected to induce a greater aerodynamic penalty, resulting in a more substantial increase in drag and, consequently, power demand.

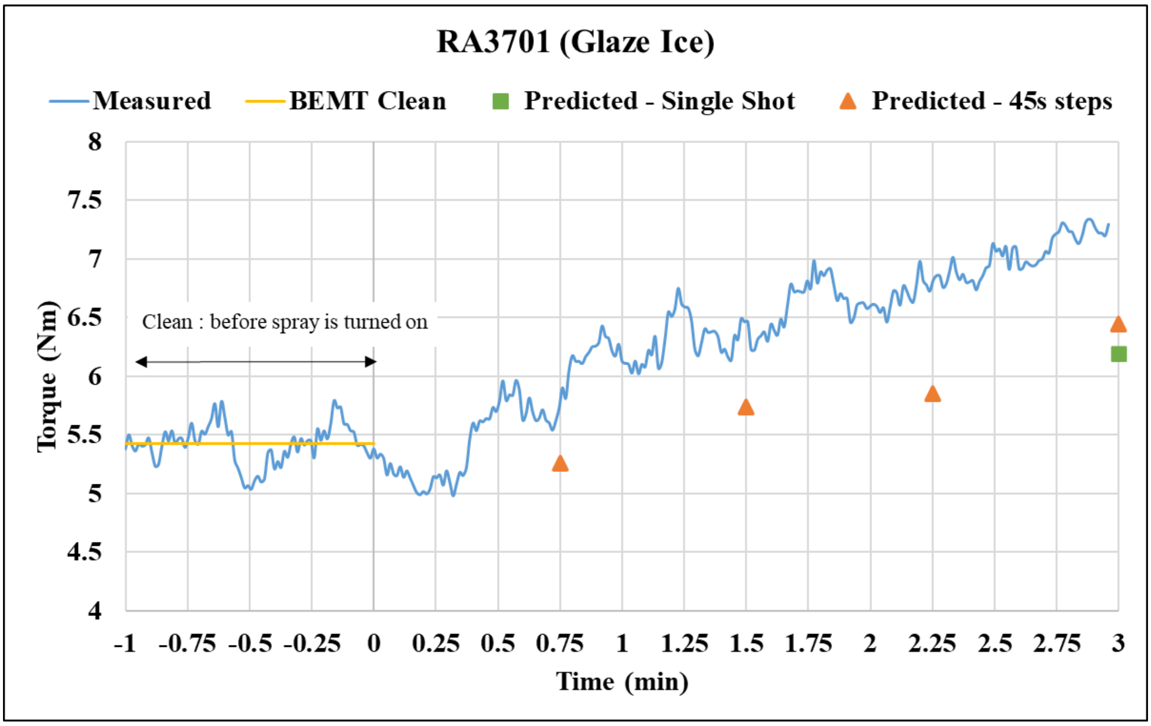

Figure 18. Comparison of measured torque with the predicted increase in torque for icing case RA3701.

CFD solution of the experimental ice shape (rime ice)

High-fidelity computational fluid dynamics (CFD) simulations were conducted using the two-dimensional Reynolds-Averaged Navier–Stokes (RANS) solver DSS2 on the experimentally measured ice shapes at 75 % span for both rime- and glaze-ice cases.

For the rime ice measured geometry (Figure 6), the flow field solution reveals the presence of recirculating regions within the ice-induced surface ridges. Figure 19 presents the contour of velocity magnitude, non-dimensionalized by the local speed of sound, along with velocity vectors and streamlines to emphasize regions of flow reversal. Notably, the flow accelerates over the peak of the most prominent ridge, resulting in a strong adverse pressure gradient immediately downstream.

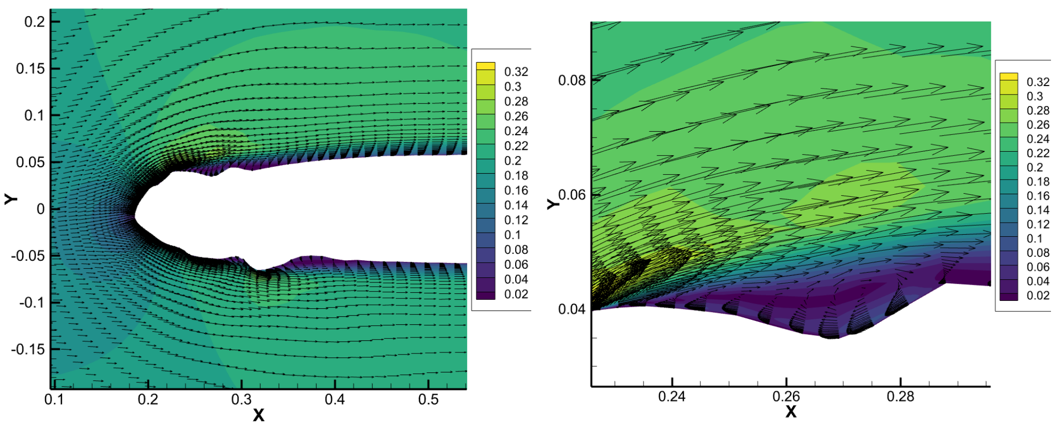

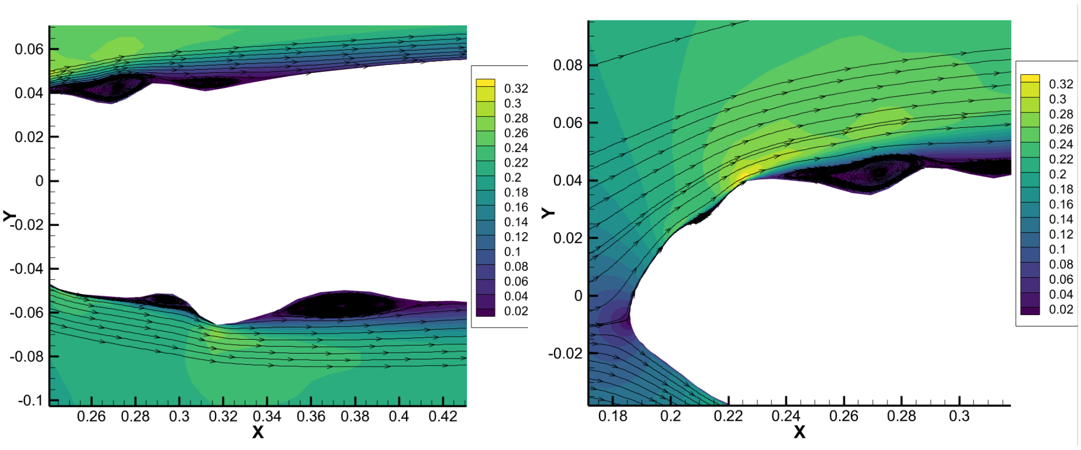

Figure 19. Mach-number contours (normalized by local speed of sound) with velocity vectors and streamlines over the experimentally measured rime-ice shape at 75 % span.

Figure 20 compares the surface pressure coefficient (Cp) distribution of the experimental ice shape at 75% span obtained from the DSS2 CFD analysis with that from predicted ice shape using XFOIL for the rime ice case. The experimental shape exhibits a sharper suction peak, whereas XFOIL underpredicts that peak; however, the integrated pressure-recovery area under both curves remains somewhat similar, suggesting that XFOIL captures the overall rime ice behavior pretty well but misses local extremes.

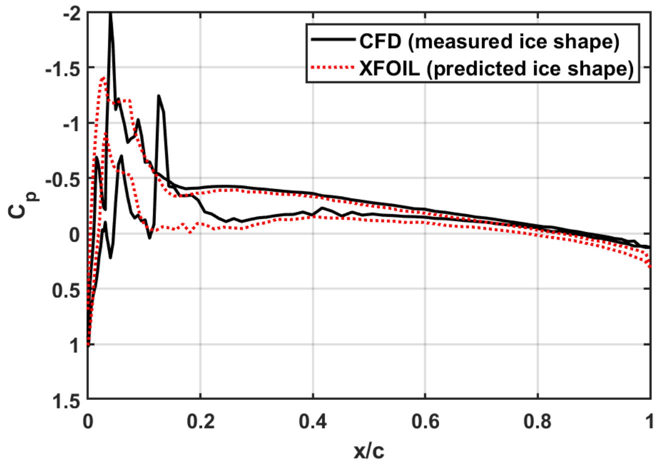

Figure 20. Surface pressure-coefficient distribution at 75 % span: DSS2 CFD on measured rime-ice shape versus XFOIL on predicted rime-ice profile.

<u>CFD solution of the experimental ice shape (glaze ice)</u>

Figure 21 presents Mach-number contours and streamlines for the experimental glaze-ice shape at 75 % span. Separation regions due to the abrupt, horn-like features are larger and more intense than in the rime-ice case, consistent with the increased aerodynamic penalty.

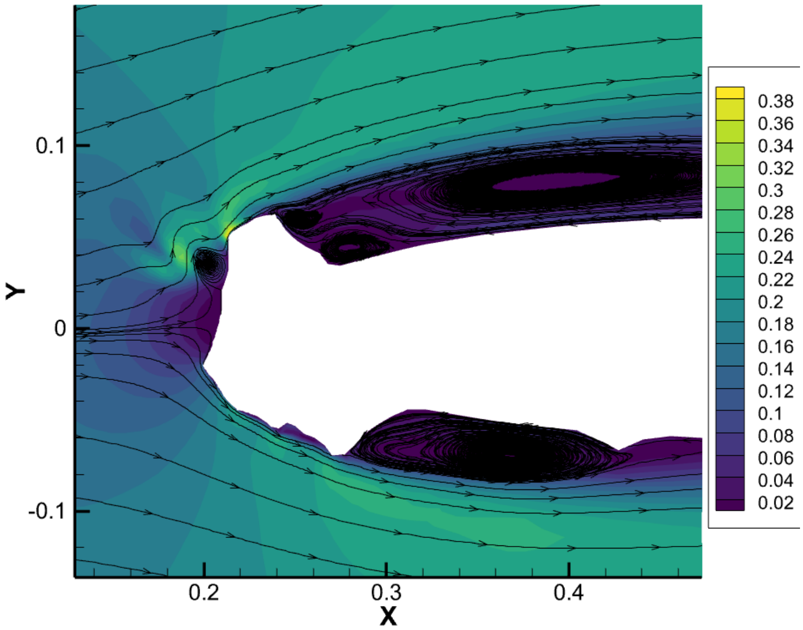

Figure 21. Mach-number contours (normalized by local speed of sound) with streamlines over the experimentally measured glaze-ice shape at 75 % span.

CFD solution of the predicted ice shape (glaze ice)

Figure 22 presents Mach-number contours and streamlines for the predicted glaze-ice shape at 75% span. As discussed previously (see Figure 10), while the simulated shape broadly reflects the overall experimental ice accretion, it fails to replicate the abrupt, horn-like features observed in the actual ice accretion.

As a result, the predicted flow in Figure 22 shows only a small separation bubble that re-attaches quickly. In contrast, the experimental shape, characterized by prominent horn-like features, produces a large region of sustained flow separation (Figure 21). This reduced separation in the predicted case leads to a smaller aerodynamic penalty, which in turn results in a less pronounced rise in power requirement compared to the experimental case. Improvements in the glaze ice shape prediction, particularly the sharp protruding horns, may lead to more accurate estimates of performance degradation in iced conditions.

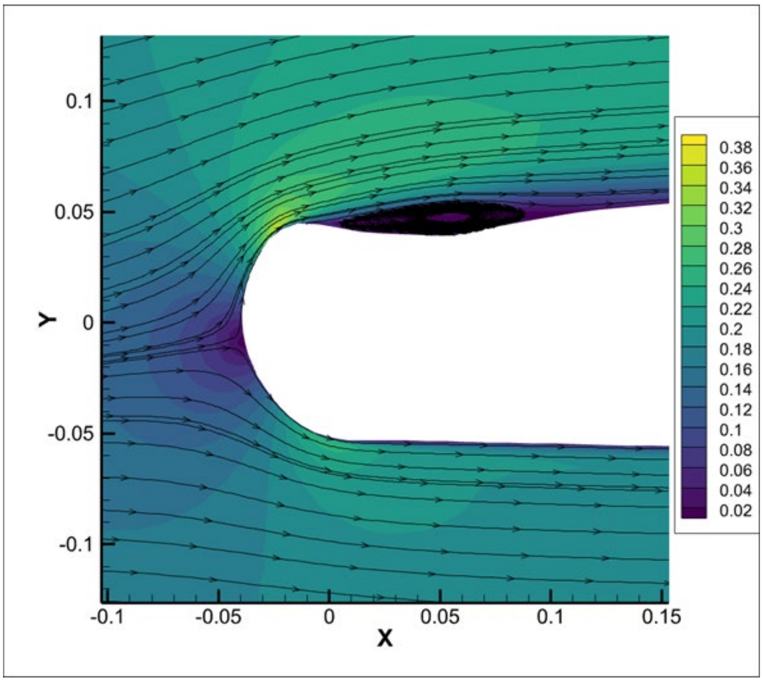

Figure 22. Mach-number contours (normalized by local speed of sound) with streamlines over the experimentally measured glaze-ice shape at 75 % span.

Figure 23 compares the surface pressure coefficient (Cp) distribution of the experimental ice shape at 75% span obtained from the DSS2 CFD analysis with that from predicted ice shape using XFOIL for the glaze ice case. The measured glaze-ice surface induces an abrupt pressure rise downstream of the ice horns, a feature absent in the XFOIL result, explaining the larger performance degradation seen experimentally.

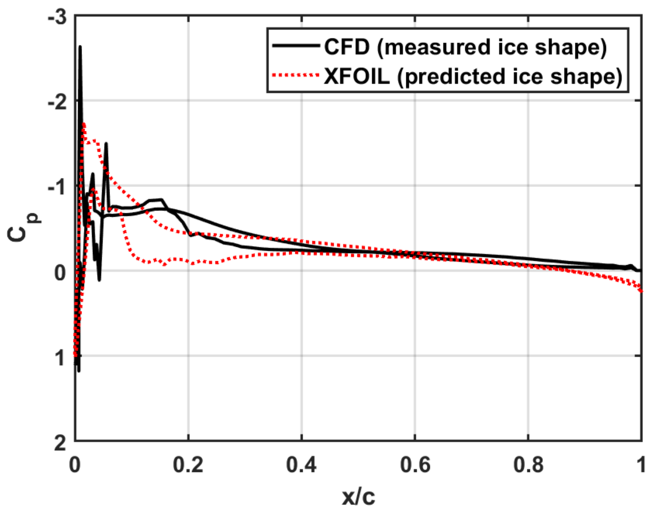

Figure 23. Surface pressure-coefficient distribution at 75 % span: DSS2 CFD on measured glaze-ice shape versus XFOIL on predicted glaze-ice profile.

SUMMARY AND CONCLUSIONS

A low-fidelity modeling framework was developed to predict performance degradation resulting from ice accretion on an eVTOL propeller. Simulated ice accretions and the resulting torque rise were compared to experimental data obtained from an eVTOL propeller tested at the NASA IRT. Two conditions were explored: a rime ice condition and a glaze ice condition. For the rime ice case, the predicted ice accretions and resulting torque rise showed relatively good agreement with experimental measurements. In contrast, the glaze ice predictions were only qualitatively accurate and significantly underpredicted the resulting torque rise. This may be attributed to the difficulty in accurately capturing some of the flow-separating features of the glaze ice shape which were not present in the simulated ice shapes.

More work is needed to understand if the accuracy of the predicted performance losses would improve had the glaze features been better captured by the simulated ice shapes. The current body-fitted grid approach may not adequately capture the complex, ragged geometries typical of glaze ice accretion. In such cases, unstructured grids or alternative meshing techniques may offer better fidelity, as they are more capable of resolving sharp features and flow separation. Addressing these aspects could lead to improved prediction of aerodynamic penalties across a broader range of icing conditions. Multiple definitions for transition based on surface roughness exist. Further studies are needed to correctly predict the transition location and the resultant rise in profile drag, especially during the early stages of rime ice formation.

Given that eVTOL rotors are designed with limited thrust and power margins, they are unlikely to operate safely under conditions where ice-induced performance penalties lead to substantial thrust loss or power increase. As a result, the allowable exposure time to icing conditions is expected to be short, potentially less than five minutes.

The performance degradation results indicate that, by the end of the icing period, both single-shot and multi-shot accretion approaches yield comparable losses if the exposure time is small (~ less than 5 minutes). Therefore, for short-duration icing encounters, a single-shot modeling approach may offer a more computationally efficient alternative that produces comparable results.

ACKNOWLEDGEMENTS

This research is partially funded through the U.S. Army/Navy/NASA Vertical Lift Research Center of Excellence at Georgia Tech under the direction of Mahendra Bhagwat of the US Army Futures Comment, Agreement No. W911W6-21-2-0001. Opinions, interpretations, conclusions, and recommendations are those of the authors and are not necessarily endorsed by the United States Government.

REFERENCES

1. Narducci, R., Liu, J., Wells, A., Mobley, F., and Mayer, R., "CFD Simulations of a Hovering Tiltrotor in Ground Effect," AIAA 2024-1115, 62nd AIAA Aerospace Sciences Meeting, Orlando, FL, January 8-12, 2024.
2. Moushegian, A., "Fast High-Fidelity Analysis of a Hovering Rotor with a Dual-Solver Hybrid CFD Methodology in HPCMP CREATE-AV Helios," AIAA 2024-1116, 62nd AIAA Aerospace Sciences Meeting, Orlando, FL, January 8-12, 2024.
3. Gahlot, A., and Sankar, L., "Effects of Rain on Hover and Forward Flight Performance of the S-76 Rotor," AIAA 2024-1117, 62nd AIAA Aerospace Sciences Meeting, Orlando, FL, January 8-12, 2024.
4. Liu, Y., and Wang, L., "High-Fidelity Simulations of Lift Cruise VTOL Urban Air Mobility Concept Aircraft in Hover," AIAA 2024-1118, 62nd AIAA Aerospace Sciences Meeting, Orlando, FL, January 8-12, 2024.
5. Jain, R, "CFD-CSD Pre-test Hover Predictions Validation for the HVAB Rotor," AIAA 2024-0893, 62nd AIAA Aerospace Sciences Meeting, Orlando, FL, January 8-12, 2024.
6. Wright, W. B., "User Manual for LEWICE Ver. 3.2," NASA CR 214255, Cleveland, OH, 2008.
7. Gupta, A., Sankar, L., and Kreeger, R., "Ice Accretion Studies Using Tools Developed at Georgia Tech and Comparisons with LEWICE " presented at the 1st AIAA Ice Prediction Workshop 2021. [Online]. Available: https://icepredictionworkshop.wordpress.com/results/.
8. Bourgault-Côté, S., Laroche, H. P., Blanchet, M., Laurendeau, E., Cook, D., Radenac, E., Broeren, A., and Potapczuk, M. G., "Code-to-code Comparisons, "presented at the AIAA 1st Ice Accretion Prediction Workshop, 2021. [Online]. Available: https://icepredictionworkshop.wordpress.com/results/
9. Kreeger, R. E., Sankar, L. N., Nucci, M., and Kunz, R., "Progress in Rotorcraft Icing

Computational Tool Development," SAE Technical Paper 2015-01-2088, 2015, doi:10.4271/2015-01-2088.
10. Von Hardenberg, P.H., Flack, C.A., & Rigby, D.L. (2024). Ice Shape Analysis of an eVTOL Propeller in Forward Flight at the NASA Glenn Icing Research Tunnel. AIAA AVIATION FORUM AND ASCEND 2024.
11. Rigby, D.L., & Von Hardenberg, P.H. (2024). GlennICE Simulation of 24, 28 and 36 Inch Diameter eVTOL Propellers in Forward Flight. AIAA AVIATION FORUM AND ASCEND 2024.
12. Bourgault, Y., Boutanios, Z., and Habashi, W. G., "Three-dimensional Eulerian approach to droplet impingement simulation using FENSAP-ICE, Part 1: model, algorithm, and validation," Journal of aircraft, vol. 37, no. 1, pp. 95-103, 2000.
13. Kim, J. W., "Development of a physics-based methodology for the prediction of rotor blade ice formation," Georgia Institute of Technology, 2015.

APPENDIX A
PROPELLER MODELING METHODOLOGY

A variety of public domain tools are available for modeling and designing propellers. However, many of these tools have some limitations. For example, the XROTOR software assumes a parabolic variation of the drag coefficient with lift coefficient, with the coefficients of the parabola determined from the user specified input for the minimum drag value and the corresponding lift coefficient. Javaprop, another popular software, includes drag polars for a number of airfoils. However, it is difficult to add additional drag polars to this library.

For these reasons, a propeller analysis based on combined blade element-momentum theory (BEM) has been developed. Unlike the classical BEM model, this does not assume a linear variation of lift vs. angle of attack. The swirl losses and tip losses are automatically included, in addition to non-uniform inflow.

The methodology below is given in dimensional form for convenience. However, much of the analysis is done in non-dimensional form. All distances and velocities in the formulation shown below have been non-dimensionalized by the tip radius and the tip velocity, respectively. The blade operating parameters such as RPM and forward speed, and the geometric parameters such as the blade diameter are used only to compute the thrust force and power in dimensional form and allows the propeller to meet the performance requirements of the configuration shown in Figure 24.

Here are the basic steps of the propeller analysis.

The blade planform, i.e. the radial variation of chord non-dimensionalized by blade radius R, and twist are imported from an Excel spreadsheet. The blade is divided into segments (blade elements). For simplicity, the number of elements and the width of each blade element are based on the supplied blade geometry locations.

A range of advance ratio values and pitch settings are chosen. The advance ratio J is defined as $\frac{\boldsymbol{V_\infty}}{\boldsymbol{nD}}$ and is based on the propeller forward speed $\boldsymbol{V_\infty}$ along the shaft axis, the number of rotor revolutions per second 'n', and the rotor diameter D. For each combination of advance ratio and blade pitch settings, the thrust and power (in their non-dimensional form) are computed, by summing up the individual contributions from the blade elements. The induced inflow velocity v is initialized to zero. The swirl velocity is also initialized to zero. An iterative process is used to update these quantities at the center of each blade element as follows.

For an annulus of radius r (located at the center of a given blade element) and the corresponding element width 'dr', the thrust dT generated may be computed from momentum theory as shown in Figure 24.

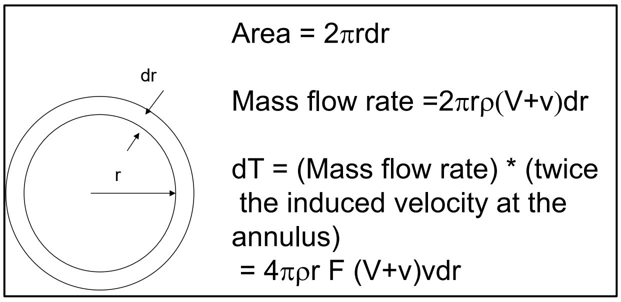

Figure 24. Thrust production over an Annulus from Momentum Theory

In this figure, the quantity F is the Prandtl's tip loss factor. In this analysis, the tip loss factor has been computed based on the radial location, the number of blades b, and the total inflow ratio λ, equal to (V+v) divided by blade tip speed ΩR, as follows:

$$\boldsymbol{F} = \frac{2}{\pi}\boldsymbol{arcCos}\left(\boldsymbol{e^{-f}}\right) \quad \text{where,} \quad \boldsymbol{f} = \frac{\boldsymbol{b}}{2}\frac{(1-\boldsymbol{r}/\boldsymbol{R})}{\boldsymbol{\lambda}} \tag{1}$$

The thrust production for each blade segment may be computed from the blade element theory, with the current values of induced velocity v, and the swirl velocity, as shown in Figure 25 below.

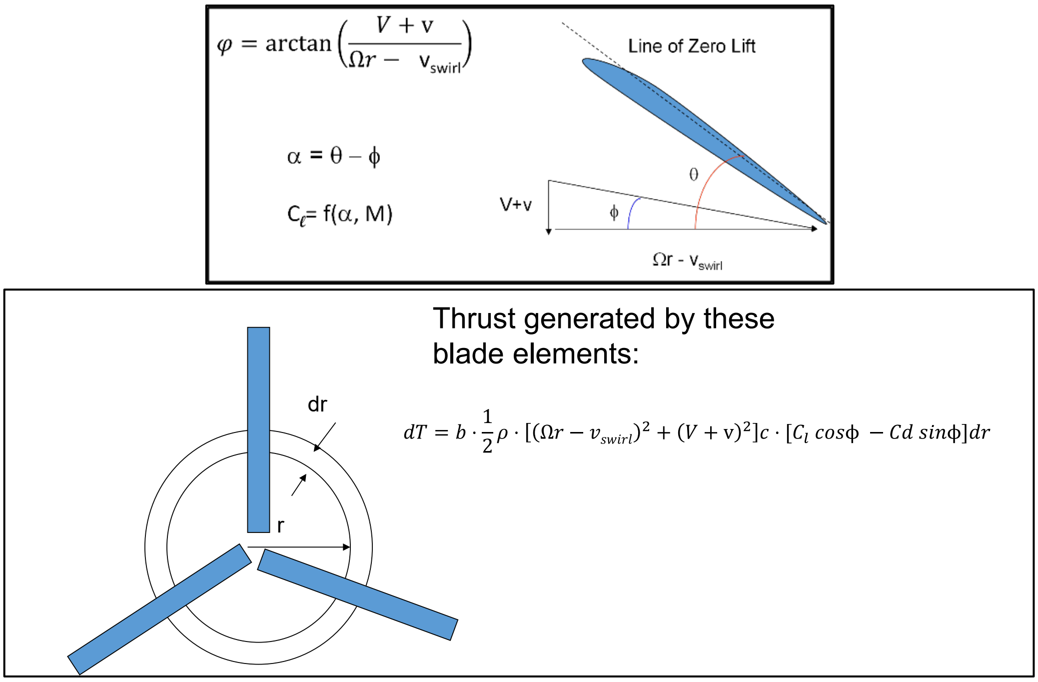

Figure 25. Thrust production over an Annulus from Blade Element Theory

Equating the thrust from the blade element theory with the corresponding value from momentum theory, the following updated estimate for the induced velocity may obtained.

$$v = \frac{bc[(\Omega r - v_{swirl})^2 + (V+v)^2](C_l cos\phi - C_d sin\phi)}{8\pi r F(V+v)}$$

(2)

In eq. (2), the righthand side is computed using the induced velocity and swirl velocity estimates at the center of the blade element from the previous iteration. The lift and drag coefficients are estimated from precomputed incompressible flow drag polars from XFOIL. The lift coefficient is corrected for compressibility effects using the Prandtl-Glauert rule.

The angular momentum associated with the swirl of the flow in the far wake, corresponding the fluid mass crossing the annulus shown in Figure 24 may similarly be expressed as

$$dQ = \rho(V+v)(2\pi r dr)\, r(2v_{swirl})$$

(3)

From blade element theory, this swirl is caused by the torque exerted by the blade elements on the fluid mass, as follows.

$$dQ = \frac{1}{2}\rho r b c[(\Omega r - v_{swirl})^2 + (V+v)^2](C_l sin\phi + C_d cos\phi)$$

(4)

Equating these two expressions, the following update for the swirl velocity may be obtained.

$$v_{swirl} = \frac{bc[(\Omega r - v_{swirl})^2 + (V+v)^2](C_l sin\phi + C_d cos\phi)}{8\pi r(V+v)}$$

(5)

In this equation, the right-hand side is computed using the estimates of the induced and swirl velocities from the previous iteration. The tip loss factor shown in equation (1) is also updated at each iteration.

When the iterations have converged, the contributions of the thrust and torque from the individual blade elements may be summed up, and multiplied by the number of blades, to compute the total thrust or torque (or power).

APPENDIX B
ICE ACCRETION MODELING METHODOLOGY

GT-ICE is an in-house ice accretion solver developed at Georgia Tech [13], based on the extended Messinger model. While the classical Messinger model relies on a one-dimensional equilibrium energy balance, it assumes uniform temperature across the water and ice layers, neglecting internal temperature gradients. This simplification leads to an underestimation of ice growth rates, particularly in glaze ice conditions, due to its use of an average layer temperature and a freezing fraction lower than the actual value.

In contrast, the extended Messinger model implemented in GT-ICE accounts for temperature gradients within both the ice and water layers. It solves a set of first-order ordinary differential equations describing the temperature distribution across these layers and applies the Stefan condition at the ice-water interface to capture the phase change dynamics. While it retains the core terms of the classical model, the extended formulation provides greater physical fidelity without sacrificing computational efficiency, making it suitable for integration into existing icing prediction frameworks.

Figure 26 illustrates the heat transfer mechanisms, and the nomenclature used in GT-ICE. Here, B(t) denotes the ice layer thickness and h(t) the water film thickness, Θ(z,t) the temperature distribution in the water layer, and T(z, t) represents the temperature profile in the ice layer.

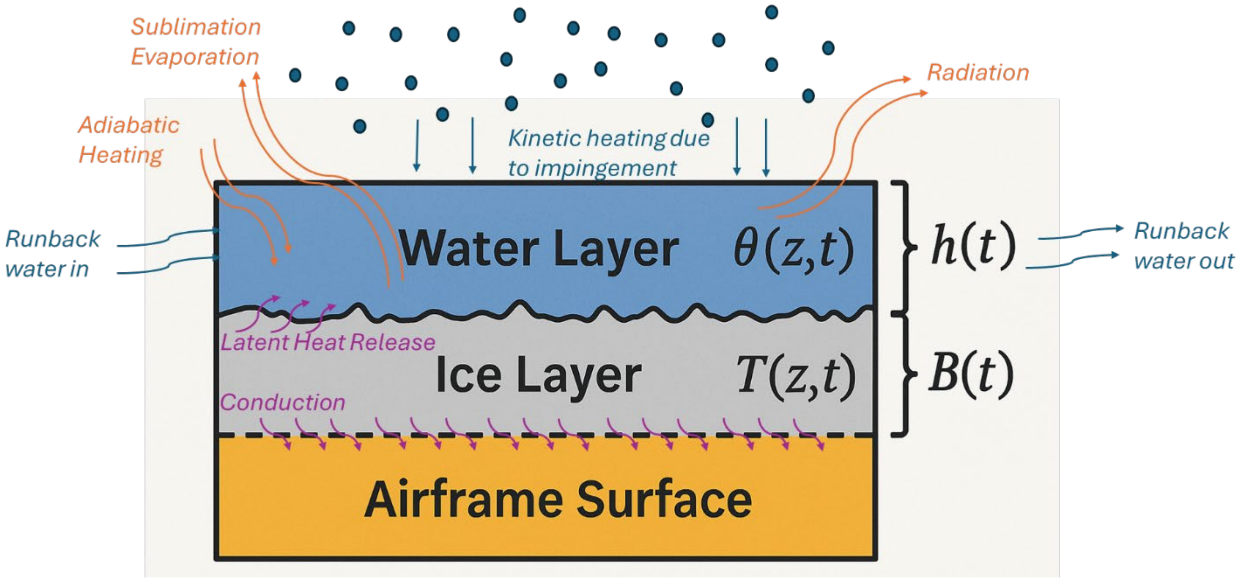

Figure 26. Heat Transfer schematic of the ice accretion.

The extended messenger model involves solving the following set of governing equations:

$$\frac{\partial T}{\partial t} = \frac{k_i}{\rho_i C_{pi}} \frac{\partial^2 T}{\partial z^2} \tag{6}$$

$$\frac{\partial\theta}{\partial t} = \frac{k_w}{\rho_w C_{pw}} \frac{\partial^2\theta}{\partial z^2} \tag{7}$$

$$\rho_i \frac{\partial B}{\partial t} + \rho_w \frac{\partial h}{\partial t} = (LWC)\beta V_\infty + \dot{m}_{in} - \dot{m}_{e,s} \tag{8}$$

$$\rho_i L_F \frac{\partial B}{\partial t} = k_i \frac{\partial T}{\partial z} - k_w \frac{\partial\theta}{\partial z} \tag{9}$$

Equation 6 and 7 are the heat conduction equations for ice and water layer respectively, where C_{pi} and C_{pw} are the value of the specific heats of ice and water respectively. ρ_i and ρ_w are the densities of ice and water respectively, k_i and k_w are the thermal conductivities of ice and water respectively.

Equation 8 is the mass balance equation, equating the growth rate of ice and water layer on the left hand side of the equation to the mass flow rate due to impingement ($(LWC)\beta V_\infty$) and mass flow rate due to the runback mass flow in from the upstream cell ($\dot{m}_{in}$) and mass flow rate out due to evaporation and/or sublimation ($-\dot{m}_{e,s}$). β is the collection efficiency, LWC is the liquid water content, V_∞ is the freestream velocity.

Equation 9 is the phase change Stefan condition at the interface of ice-water layer. In this equation L_F is the latent heat of fusion i.e the amount of energy required to change a substance from solid to liquid form. The left-hand side of the equation is the energy flow rate (per unit area) available to form ice ($\rho_i L_F \frac{\partial B}{\partial t}$) and is equal to the difference between the rate of energy absorbed by the ice layer ($k_i \frac{\partial T}{\partial z}$) and the rate of energy released by water layer.

The assumptions are as follows:

- T(0,t) = Ts , the temperature at the ice-airframe interface is assumed to be constant and equal to the ambient surface temperature. This implies perfect thermal contact between the ice and the airfoil surface, which is valid for metallic surfaces with high thermal conductivity and significantly greater thermal mass than the accreted ice. This assumption may be relaxed if a variable surface temperature is provided as an input to the icing model.

- T(B,t) = θ(B,t) = Tf , the temperature at the ice-water interface is assumed to be constant and equal to the freezing temperature, Tf.

- Radiation boundary condition with added heat flux is applied at the air-water interface. The net surface heat flux includes contributions from convection (Q), radiation (Qr), latent heat release (Ql), cooling from incoming droplets (Qd), heat input from runback water (Qin), evaporation (Qe) or sublimation (Qs), aerodynamic heating (Qa), and the kinetic energy of impinging droplets (Qk), as depicted in the schematic in Figure 23.

- B = h = 0, t = 0, i.e the initial thicknesses of the ice and water layers are zero at t=0, indicating a clean surface at the onset of icing.

- The physical properties of ice and water are assumed to be constant with temperature. Ice density is held fixed but can assume one of two discrete values depending on whether rime or glaze ice forms. The transition between these regimes is assumed to occur instantaneously. In the governing equations, the ice density, ρ_i, is assigned either ρ_r = 880 kg/m^3 for rime ice or ρ_g = 917 kg/m^3 for glaze ice.

- Phase changes are assumed to occur at a single freezing temperature, Tf = 273.15 K.

The nine different energy terms appearing in the heat exchange are summarized in table 4 below:

Table 4. Summary of heat flux terms utilized in ice accretion module

Convection	$Q_c = h_c(T - T_a)$
Radiation	$Q_r = 4\varepsilon\sigma_r T_a^3(T - T_a)$
Latent heat release	$Q_l = \rho_r L_F \frac{\partial B}{\partial t}$
Cooling by incoming droplets	$Q_d = LWC\,\beta V_\infty C_{pw}(T - T_a)$
Heat brought in by runback water	$Q_{in} = \dot{m}_{in} C_{pw}(T_f - T)$
Evaporation heat loss	$Q_e = \chi_e e_0(T - T_a)$
Sublimation heat loss	$Q_s = \chi_s e_0(T - T_a)$
Aerodynamic Heating	$Q_a = \frac{r h_c V_\infty^2}{2C_p}$
Kinetic heating due to incoming droplets	$Q_k = \frac{(LWC)\beta\, V_\infty^3}{2}$

The derivation, implementation and the constant parameter values used in the equations of the heat flux terms can be found in Reference 13. The radiation boundary condition with the added heat flux at the air-water interface for the rime ice computation at z = B is applied as,

$$-k_i \frac{\partial T}{\partial z} = (Q_c + Q_s + Q_d + Q_r) - (Q_a + Q_k + Q_{in} + Q_l) \tag{10}$$

The radiation boundary condition for the glaze ice case at z = B + h, as expressed in equation 11,

$$-k_w \left.\frac{\partial \theta}{\partial z}\right|_{z=B+h} = (Q_c + Q_e + Q_d + Q_r) - (Q_a + Q_k + Q_{in}) \tag{11}$$

The four governing equations, together with the associated boundary conditions, yield expressions for the ice thickness in both rime and glaze ice cases.

For the rime ice case, a straightforward integration of the mass conservation equation (Eq. 8) leads to an expression for the ice thickness. Since there is no water layer present in rime ice conditions, the second term on the right-hand side of Eq. 8 becomes zero (h=0). The resulting expression for rime ice thickness is:

$$B = \left(\frac{(LWC)\beta V_\infty + \dot{m}_{in} - \dot{m}_s}{\rho_r}\right) t + B(0) \tag{12}$$

Where, B(0)=0, reflecting the assumption of an initially clean surface.

Similarly, for the glaze ice case, an expression for ice thickness can be derived; however, the formulation is more complex due to the coupled nature of the governing equations. The presence of a water layer introduces additional interdependencies between mass and energy conservation, making analytical integration non-trivial. A complete derivation is provided in Reference 13.

$$\rho_g L_F \frac{\partial B}{\partial t} = \frac{k_i(T_f - T_s)}{B} + \frac{k_w\left[(q_c + q_e + q_d + q_r)(T_f - T_a) - (Q_a + Q_k + Q_{in})\right]}{k_w + h(q_c + q_e + q_d + q_r)} \tag{13}$$

This equation may be integrated with respect to time using a fourth-order Runge-Kutta scheme.

The thickness of the water layer is determined from the mass conservation equation. Upon integrating over time, the water film thickness can be expressed as,

$$h(t) = \left[\frac{(LWC)\beta V_\infty + \dot{m}_{in} - \dot{m}_{e,s}}{\rho_w}\right](t - t_g) - \frac{\rho_g}{\rho_w}(B - Bg) \tag{14}$$

In this expression, Bg and tg represent the thickness of ice and the corresponding time at which glaze ice first begins to form. At this instant, the water layer height is zero, i.e., h(tg)=0. Substituting this condition into the mass conservation equation allows for the derivation of an expression for Bg, the ice thickness at the onset of glaze ice formation.

$$B_g = \frac{k_i(T_F - T_s)}{L_F\left[(LWC)\beta V_\infty + \dot{m}_{in} - \dot{m}_{e,s}\right] + (Q_a + Q_k + Q_{in}) - \left[(q_c + q_e + q_d + q_r)(T_f - T_a)\right]} \tag{15}$$

The time at which glaze ice first appears, tg, can be simply calculated by equating the ice thickness at the onset of glaze ice formation, equation 15, to the rime ice thickness, equation 12.

$$t_g = \left[\frac{\rho_r}{(LWC)\beta V_\infty + \dot{m}_{in} - \dot{m}_{e,s}}\right] B_g \tag{16}$$

Equations (15) and (16) illustrate how the onset of glaze ice formation, represented by the critical ice thickness Bg and the corresponding time tg, depends sensitively on ambient and surface conditions. Notably, the expression for Bg may yield positive, negative, or even infinite values, each with distinct physical implications:

- When $0 < Bg < \infty$, the solution represents a physically meaningful ice thickness at which glaze ice first appears, and the corresponding time tg can be computed using Equation (16).
- A negative value of Bg indicates that glaze ice cannot form. This occurs when the numerator of Equation (15) becomes negative—i.e., when $Tf - Ts < 0$ implying that the surface or substrate is warmer than the freezing point, thereby inhibiting ice growth.
- If the denominator of Equation (15) is zero or negative, the resulting Bg becomes infinite or undefined. This suggests that the available energy flux is insufficient to sustain a liquid water layer, and the system produces only pure rime ice.

Thus, the model captures the transition between rime and glaze ice regimes and determines the conditions under which each ice type is expected to form.

In order to find the runback rate out, as shown in figure 23, freezing fraction (FF) needs to be computed. It quantifies the proportion of water that freezes within a given control volume. It is defined as the ratio of the mass of water that solidifies (as either rime or glaze ice) to the total mass of water available in the control volume, which includes both impinging water and any incoming runback water from upstream cell.

For rime ice, where only solidification occurs and no liquid film forms, the freezing fraction is given as,

$$FF = \frac{\rho_r B}{((LWC)\beta V_\infty + \dot{m}_{in})t} \tag{17}$$

For glaze ice, where both rime and glaze ice may form due to the presence of a water film, the freezing fraction accounts for both types of ice, as,

$$FF = \frac{\rho_r B + \rho_g (B - B_g)}{((LWC)\beta V_\infty + \dot{m}_{in})t} \tag{18}$$

The runback mass flow rate, the amount of water that does not freeze and flows downstream, is then expressed as,

$$\dot{m}_{out} = (1 - FF)\big((LWC)\beta V_\infty + \dot{m}_{in}\big) - \dot{m}_e \tag{19}$$

This outflow becomes the incoming runback water m_{in} for the adjacent downstream control volume, coupling the icing process across the surface.

Finally, evaporation or sublimation losses from the surface are computed using vapor pressure differences between the ice or water surface and the ambient air.

$$\dot{m}_{e,s} = \frac{0.7}{C_{pa}} h_c \left(\frac{p_{v,sur} - p_{v,\infty}}{p_\infty}\right) \tag{20}$$

The mass loss rate is derived from empirical correlations involving vapor pressure p_v, calculated as,

$$p_v = 3386(0.0039 + 6.8096e - 6\bar{T}^2 + 3.5579e - 7\bar{T}^3) \tag{21}$$

with temperature in Fahrenheit expressed as,

$$\bar{T} = 72 + 1.8(T - 273.15) \tag{22}$$

APPENDIX C
ICE ACCRETION IMAGES FROM EXPERIMENT

(a) (b)

Figure 27. Ice Accretions on the (a) Pressure and (b) Suction Side of the Blade for Run RA3683

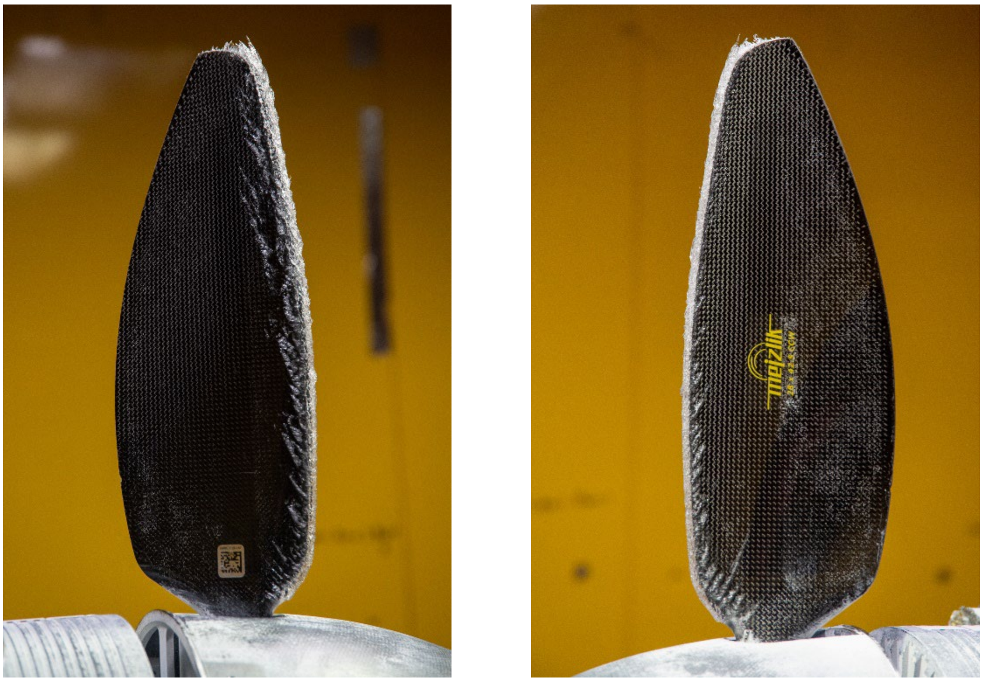

(a) (b)

Figure 28. Ice Accretions on the (a) Pressure and (b) Suction Side of the Blade for Run RA3701